Particle trapping and ponderomotive processes during breaking of ion acoustic waves in plasmas

Bharati Kakad,[1,a)] Amar Kakad,[1,b)] and Yoshiharu Omura[2,c)]
[1]*Indian Institute of Geomagnetism, New Panvel, Navi Mumbai 410-218, India*
[2]*Research Institute for Sustainable Humanosphere, Kyoto University, Uji, Kyoto 611-0011, Japan*

(Received 1 June 2017; accepted 20 September 2017; published online 5 October 2017)

Recent fluid simulations show that the ponderomotive potentials and ponderomotive frequencies of electrons and ions can be used as proxies to identify steepening and breaking of the ion acoustic solitary waves (IASWs) in plasmas. However, the behavior of these proxies may deviate in the presence of kinetic effects such as particle trapping. We performed one-dimensional particle-in-cell (PIC) simulations to examine the effects of kinetic processes on the behavior of these proxies at the breaking of IASWs in plasmas. The electron and ion equilibrium densities were superimposed by a long-wavelength Gaussian type perturbation, which initially evolves into two IASWs observed as two phase space vortices due to the trapping of electrons in the ion acoustic (IA) potentials. These IASW structures grow due to the steepening of their trailing edges, and later they break into a chain of IA phase space vortices. Each of these vortices is associated with a bipolar electric field resulting in a positive potential structure. We examined the amplitude, width, and phase velocity of the IASWs at their breaking process to clarify their link with the trapping velocity. In addition, we estimated electron and ion ponderomotive potentials and frequencies from the PIC simulations to verify their applicability in identifying wave breaking limit under the kinetic regime. The present study shows that the behavior of the ponderomotive potential during the IA wave breaking process is similar to the one, which is proposed through fluid simulations. We find that IA wave breaking occurs when the maximum trapping velocity of the electron ($V_{trap} + V_s$) exceeds its thermal velocity. The present simulation study shows that both maximum electron trapping velocity and ponderomotive potential can be used to identify the IA wave breaking processes in plasmas. *Published by AIP Publishing.* https://doi.org/10.1063/1.4986030

I. INTRODUCTION

Phenomena of the breaking of large amplitude waves and oscillations in a plasma have been a focus of research for a long time. This phenomenon serves as a useful paradigm to illustrate the physics of many plasma-based processes, e.g., wave energy dissipation, particle heating,[1] etc. in laboratory and space plasma environments, where nonlinear waves/oscillations are excited. Any nonlinear propagating wave in a plasma has a fundamental limitation imposed by the wave breaking threshold. The wave breaking can either completely destroy the regular structure of the wave, or it can develop quite gently, with only a small portion of the wave involved in the break. The hydrodynamic investigations of wave breaking were first undertaken for cold plasmas,[2,3] and thermal effects were later included in nonrelativistic[4–7] and relativistic contexts.[8–10] It is clear from all these models that the electric field at which the wave breaks (i.e., the electric field's 'wave breaking limit') is highly sensitive to the details of the hydrodynamic model. The traditional criterion for the wave breaking in plasma is established based on the critical amplitude and the phase velocity of the breaking wave. For both nonrelativistic and relativistic cold plasmas, the wave breaking happens when the peak fluid velocity equals the phase velocity of the plasma wave.[2,3]

In warm plasmas, the breaking of ion acoustic (IA) waves has been studied by a number of researchers.[11–16] Judice *et al.*[12] performed a hybrid simulation that treats ions as finite-size particles, and electrons as an isothermal fluid to study the breaking and turbulent transition in IA waves. A Vlasov simulation was performed to study the disintegration of an initial density perturbation (IDP) into a number of ion acoustic solitary waves (IASWs) in the presence of the trapping effect of electrons.[17] The formation of chain of IASWs through the process of wave breaking and their collision is examined using particle-in-cell (PIC) simulations.[18] However, their aim was to investigate the particle dynamics and stability of IASWs during the head on collision of multiple electron vortices linked with these IASWs. Recently, Kakad and Kakad[16] carried out a fluid simulation of the breaking of IASWs. They proposed that the ponderomotive potential and ponderomotive frequencies of electrons and ions could be used as proxies to determine the steepening and breaking time of the IASWs. However, these proxies might behave differently in the presence of kinetic effects such as particle trapping. In the present paper, we perform particle-in-cell (PIC) simulations to examine the behavior of the ponderomotive potential at the breaking of the IASWs in a plasma under the kinetic regime. In Sec. II, we present the PIC simulation model. Generation of IASWs and their

[a)]ebharati@iigs.iigm.res.in
[b)]amar@iigs.iigm.res.in
[c)]omura@rish.kyoto-u.ac.jp

breaking is discussed in Sec. III A. The role of particle trapping and ponderomotive processes involved in the breaking of the IASWs is discussed in Secs. III B and III C, respectively. The energy exchange and particle acceleration at the breaking of the IASWs are discussed in Sec. III D. Finally, the results are summarized in Sec. IV.

II. PLASMA SIMULATION MODEL

We have used a one-dimensional electromagnetic PIC code based on the Kyoto university ElectroMagnetic Particle Code (KEMPO).[18–21] In this code, Maxwell's equations and equations of motion are solved for a large number of superparticles.[22] At each time step, we update the field values defined at each grid point by solving Maxwell's equations with the standard finite-difference time domain (FDTD) method. The obtained fields are then used in the equations of motion for updating the particle velocities and positions in time. We use the Buneman-Boris method[19] for updating particle velocities. The variation of fields defined at grid points and dynamics of plasma constituent located at arbitrary positions are updated in a self-consistent manner. In this code, the initial velocity distributions of the particles are assumed to be shifted-Maxwellian distribution given by

$$f_j(v) = \frac{n_j}{\sqrt{2\pi}\, V_{th\|j}} \exp\left[-\frac{(v - V_{d\|j})^2}{2V_{th\|j}^2}\right], \tag{1}$$

where the subscripts $j = e$, i represent the electrons and ions, respectively. The parameters $V_{th\|j}$, $V_{d\|j}$, and n_j represent the thermal velocity, drift velocity parallel to the magnetic field and number density of species j, respectively.

This PIC code can be used for both electrostatic and electromagnetic simulations. For the electrostatic case, the code solves Poisson's equation for the electric field. This field is then used in the equations of motion for updating the particle velocities and positions in time. We assume nondrifted electrons and protons ($V_{de} = V_{di} = 0$) in the simulation system with the periodic boundary conditions. The parameters for the simulation runs are given in Table I. We perform the simulation for two different electron thermal velocities, i.e., $V_{th\|e} = 65$ (Run-1) and 50 (Run-2) by keeping the ion thermal velocity $V_{th\|i} = 0.5$, which corresponds to the electron to ion temperature ratio, $T_e/T_i = 169$ and 100, respectively. We perturbed the equilibrium electron and ion densities with the standard Gaussian perturbation as given by the following equation:

$$n_j(x) = n_{j0} + \Delta n \ \exp\left(-\frac{(x - x_c)^2}{l_0^2}\right). \tag{2}$$

In the equation above, n_{j0} is the equilibrium density of the species j. Here, $j = e$ for electrons and i for ions. The parameters Δn and l_0 give the amplitude and width of the superimposed density perturbation. Here x_c is the center of the simulation system, i.e., $L_x/2$, where the perturbation is introduced. The superparticles (n_p) in the simulation system are distributed such that they satisfy the distribution described above.

TABLE I. Parameters used in PIC simulations.

Parameters	Run-1	Run-2
$V_{th\|\|e}$	65	50
$V_{th\|\|i}$	0.5	0.5
T_e/T_i	169	100
$V_{di} = V_{de}$	0	0
λ_{di}	0.5	0.5
ω_{pi}	1	1
ω_{pe}	10	10
Δn	0.5	0.5
l_0	102	102
L_x	4000	4000
dx	1	1
dt	0.002	0.002
m_e/m_i	0.01	0.01
n_p/dx/species	48 000	48 000

III. SIMULATION RESULTS

A. Evolution and breaking of IASWs

In this section, we discuss the evolution and breaking of IASWs for Run-1. The plasma with $T_e > T_i$ and no applied magnetic field supports only two electrostatic normal modes, namely a high and a low-frequency mode. The high-frequency mode is the one in which the electrons oscillate rapidly about stationary ions is the electron plasma wave or Langmuir wave. The low-frequency mode is the ion acoustic wave driven by an electric field that arises because of the space charge developed by a slight displacement between ion and electron densities. The evolution of IASWs in such a plasma depends on the wavelength of the initial density perturbation (IDP). By using fluid simulations, it is demonstrated that in such plasmas, a short-wavelength IDP evolves into two counter-propagating IASW pulses, whereas the long-wavelength perturbation evolves initially into long-wavelength IASW pulses, which later break and evolve into multiple IASW pulses in the system.[15,16]

The breaking of IASW pulses up to and beyond wave breaking is shown in Fig. 1 for Run-1. The panels in the first and second rows of this figure, respectively, show electron and ion phase space distributions at different timings, $\omega_{pi}t = 0$, 38, 62, 180, and 270. The panels in the third and fourth rows, respectively, show the evolution of particle densities and electrostatic potential in the system at corresponding times. The panels at $\omega_{pi}t = 0$ show the initial setup of the simulation when IDP is introduced in uniformly distributed superparticles. At this stage, the injection of the IDP causes charge separation in the plasma that sets up an infinitesimal electrostatic potential in the system, which grows with time to evolve into two oppositely propagating long-wavelength IASW pulses along with the IA oscillations and Langmuir waves. One of the snapshots of such IASW pulses is shown at $\omega_{pi}t = 38$. It is seen that the ions play an important role in the generation of these waves. One can see two local enhancements in the ion and electron densities linked with the two IASWs that are propagating in the opposite directions. The slower electrons get trapped into the counter-

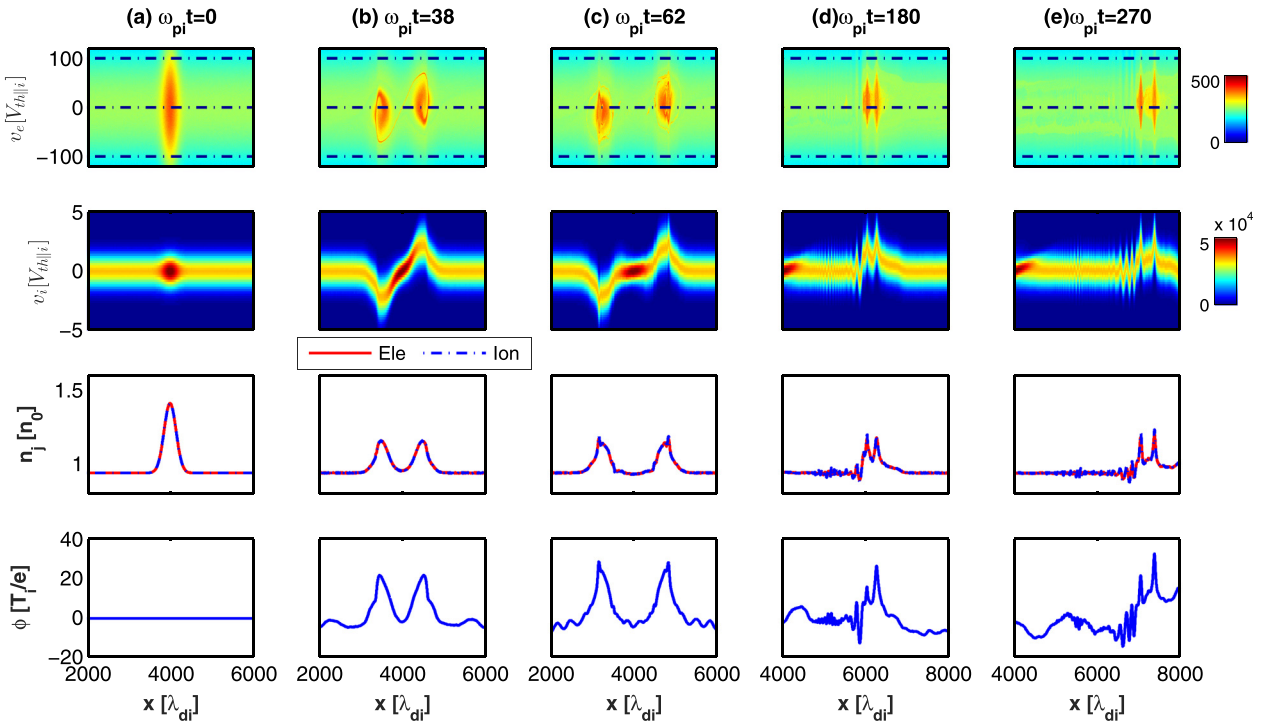

FIG. 1. Snapshots of different evolutionary stages for Run-1. Distribution of electrons (upper row) and ions (second row) in x–v space, number density of electrons and ions (third row), and electrostatic potential (fourth row) as a function of x at (a) initial time $\omega_{pi}t = 0$, (b) formation of two counter-propagating IASW structures at $\omega_{pi}t = 38$, (c) trapped electron vortices linked with IASWs starts breaking at $\omega_{pi}t = 62$, (d) two counter-propagating pairs of IASWs are formed through breaking of each of these pulses. One of the snapshots of the pulses propagating towards the right-side boundary of the simulation at around $\omega_{pi}t = 180$ is shown in this panel. (e) The IASW pulses separate from each other because of their different velocities. One of the snapshots of these pulses at $\omega_{pi}t = 270$ is shown in this panel.

propagating positive wave potentials forming electron vortices in the phase space distribution of the electrons. The ions are also found to respond as per the direction of the motion of trapped electrons in the wave potential. As a result, one hump and one dip are seen in the ion phase space distribution. During the course of the propagation, the IASW pulses move towards the simulation boundaries, both pulses acquire critical amplitude through steepening and then break. The snapshots of the phase space distributions, densities of the electrons and ions, and the electrostatic potential at the time of the initiation of the breaking of the IASW (i.e., $\omega_{pi}t = 62$) are shown in Fig. 1(c). Once the wave breaking process is initiated, IA pulses are formed one by one and get detached from each other. In this way, two structures are formed in each oppositely propagating chain of IASWs at $\omega_{pi}t = 180$. At the breaking of the IASW pulses, each of the electron vortices, and the ion humps in their respective phase space distributions also splits into two. It is noticed that the amplitudes of the leading IASW pulses are relatively greater than those of the subsequent IASW pulses. After a sufficient time at $\omega_{pi}t = 270$, these IASW structures are well separated from each other because of their different phase velocities. Subsequently, two chains of counter-propagating IASWs form in the system. The IASWs in both oppositely propagating chains are distinguishable and they are nearly stable during their propagation. For Run-2, the evolutionary stages mentioned above are respectively observed at $\omega_{pi}t = 0$, 46, 80, 220, and 340, which are displayed in Fig. 2. It is noted that for Run-2, each chain contains three IASW pulses rather than two as observed for Run-1. It suggests that the electron thermal velocity plays an important role in deciding the number of IASWs formed through the wave breaking process. Evolution of the chain of IASWs can be seen in the attached supplementary material in the form of movie-1 and movie-2 for Run-1 and Run-2, respectively.

The spatial and temporal evolutions of the electrostatic potentials associated with different modes in both simulation runs are illustrated in Fig. 3. The initial density perturbation evolves into two oppositely propagating IASWs at $\omega_{pi}t_{F1}$, whereas at time $\omega_{pi}t_{B1}$, breaking of the IASWs starts, which later evolve into a chain of IASW pulses. It may be noted that the time of formation ($\omega_{pi}t_{F1}$) and the time of wave breaking ($\omega_{pi}t_{B1}$) are different in both simulation runs. It is found that the initial formation of IASW and its breaking occur earlier with the higher electron thermal velocity (i.e., Run-1) than in plasma with lower thermal velocity (Run-2). The criteria for identifying the time of formation and the wave breaking is based on the time variation of the ponderomotive potential in the simulation system, and it is discussed in Sec. II. It is also found that the number of coherent phase space vortices of IASWs formed in the simulation system varies with the thermal velocity of the electron. For example, when the same IDP is introduced in the simulation system, two IASWs are formed in Run-1, whereas three IASWs are generated in Run-2, through the wave breaking process. These vortices are labeled with numbers in Fig. 3. The simulation run with the higher electron temperature generates IASWs with larger amplitudes than the run with the smaller

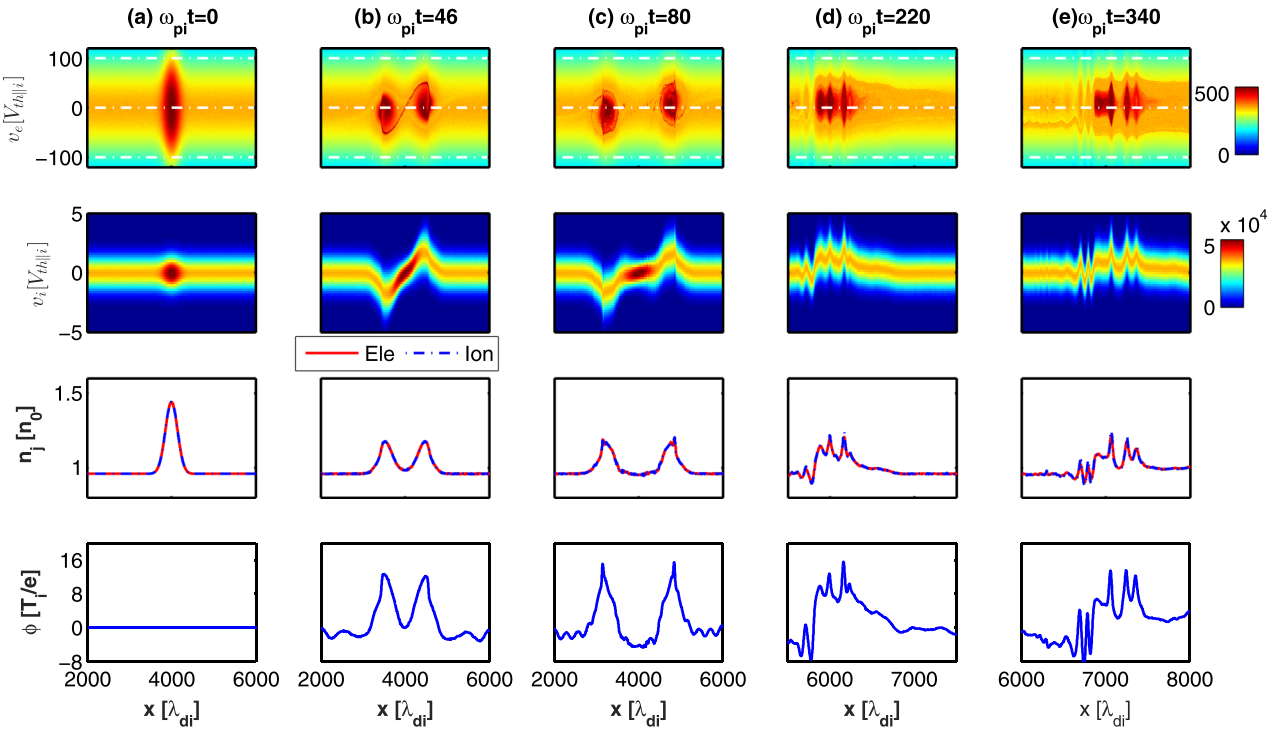

FIG. 2. Snapshots of different evolutionary stages for Run-2. Distribution of electrons (upper row) and ions (second row) in x–v space, number density of electrons and ions (third row), and electrostatic potential (fourth row) as a function of x at (a) initial time $\omega_{pi}t = 0$, (b) formation of two counter-propagating IASW structures at $\omega_{pi}t = 46$, (c) trapped electron vortices linked with IASWs starts breaking at $\omega_{pi}t = 80$, (d) two counter-propagating pairs of IASWs are formed through breaking of each of these pulses. One of the snapshots of the pulses propagating towards the right-side boundary of the simulation at around $\omega_{pi}t = 220$ is shown in this panel. (e) The IASW pulses separate from each other because of their different velocities. One of the snapshots of these pulses at $\omega_{pi}t = 340$ is shown in this panel.

electron temperature. This is similar to that of the results from the fluid simulations performed by Kakad and Kakad,[16] wherein the generation of a number of solitary pulses and their characteristics in the system is dependent on the electron temperature.

We analyze the spatial and temporal evolution of electron and ion densities associated with the IASWs for both the simulation runs; Run-1 and Run-2 in Fig. 4. We can identify the breaking of the IASWs from the spatial-temporal variation of electron and ion densities. It is seen that the number of dark yellow bands in the panels of Fig. 4 increases after initiation of the wave breaking. This shows that the initially formed unstable IA pulses break and evolve into multiple IA pulses, which are observed as two chains of stable multiple IA solitons at a later time. The dashed blue horizontal lines at $\omega_{pi}t_{F1} = 38$ and $\omega_{pi}t_{F2} = 46$ show the time at which the formation of two IASW pulses occurs in Run-1 and Run-2, respectively, whereas the dashed red horizontal lines at $\omega_{pi}t_{B1} = 62$ and $\omega_{pi}t_{B2} = 80$, respectively, show the initiation of breaking of IA waves in Run-1 and Run-2. The slope of the distinct yellow bands in Figs. 3 and 4 represents the phase velocities of the respective IASW pulses. The leading pulse in Run-1 has phase velocity $V_{s1} = 12.42V_{thi}$, whereas the later pulse has speed $V_{s2} = 11.02V_{thi}$. In Run-2, the leading pulse has $V_{s1} = 9.27V_{thi}$, followed by the second and third IASW pulses with $V_{s2} = 8.61V_{thi}$ and $V_{s3} = 8.37V_{thi}$, respectively. This implies that both phase velocities and amplitudes of the IASW pulses in the chains formed through the wave breaking are relatively higher for the plasma with the higher electron thermal velocity.

B. Particle trapping processes at the breaking of IASWs

As discussed in Sec. II, we initialize the PIC simulation by introducing the IDP in the equilibrium electron and ion

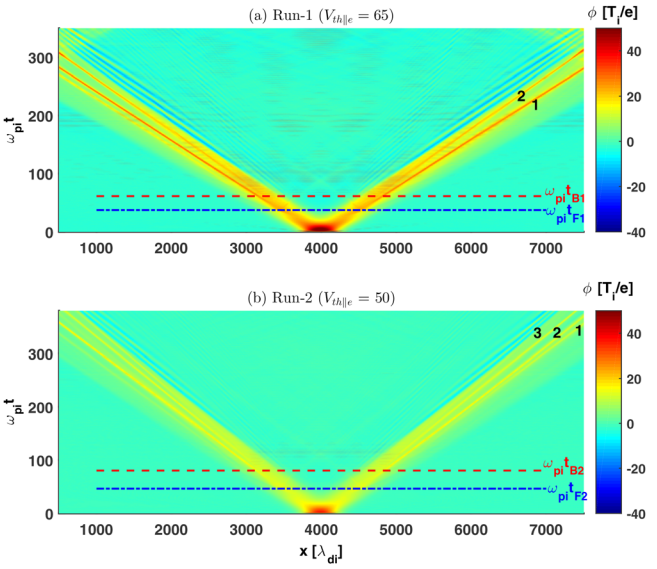

FIG. 3. Spatial and temporal evolution of electrostatic potentials for the simulation runs (a) Run-1 ($V_{th\|e} = 65$) and (b) Run-1 ($V_{th\|e} = 50$). The color bands with notations 1, 2 in the upper panel, and 1, 2, and 3 in the lower panel show propagation of the IASW structures in the simulation. The time steps at which the formation of two counter-propagating IASW pulses and initiation of their breaking are shown with the horizontal lines at $\omega_{pi}t_{F1}$ and $\omega_{pi}t_{B1}$ ($\omega_{pi}t_{F2}$ and $\omega_{pi}t_{B2}$), respectively, in Run-1 (Run-2).

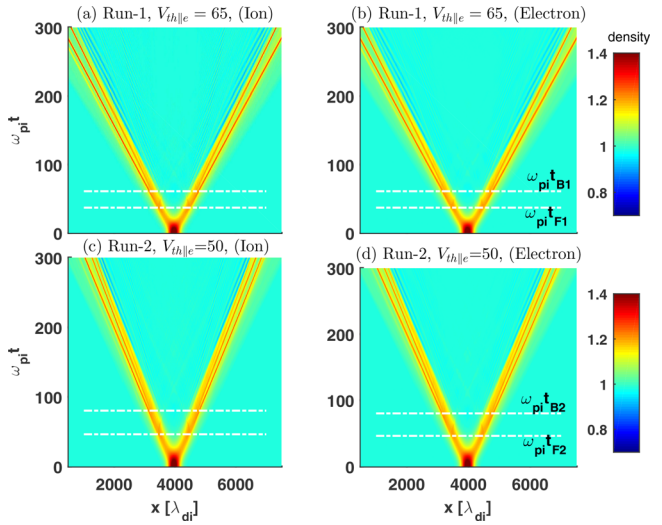

FIG. 4. Spatial and temporal evolution of electron and ion densities in the simulation runs (a) Run-1 ($V_{th\|e} = 65$), ion, (b) Run-1 ($V_{th\|e} = 65$), electron, (c) Run-2 ($V_{th\|e} = 50$), ion, and (d)Run-2 ($V_{th\|e} = 50$), electron. The dark yellow bands in the panels are associated with the evolution of IASW structures in the simulation. The time steps at which the formation of two counter-propagating IASW pulses and initiation of their breaking are shown with the horizontal dashed lines at $\omega_{pi}t_{F1}$ and $\omega_{pi}t_{B1}$ ($\omega_{pi}t_{F2}$ and $\omega_{pi}t_{B2}$), respectively, in Run-1 (Run-2).

densities. The electrons quickly respond to the perturbation, which results in the charge separation in the system, and subsequently, develops the growing positive electrostatic potential pulse. This growing potential pulse then evolves into two IASW pulses, which later break into multiple IASW pulses. Traditionally, the formation and breaking of IASW pulses are linked with the critical amplitude and phase velocity of IASW pulses.[16] The maximum electric field (E_m) associated with this positive potential as a function of time is shown in Fig. 5(a) for both runs. The varying electric field in the system modifies the trapping criteria of the electrons into the IASW potentials. We calculate the trapping velocity (V_{trap}) as a function of time in both Run-1 and Run-2. Matsumoto and Omura[23] have demonstrated the trapping of an electron by a monochromatic wave traveling parallel to the magnetic field. We calculate the trapping velocity $V_{trap} = 2\omega_{trap}/k$, where $\omega_{trap} = \sqrt{ekE_m/m_e}$ is the trapping frequency. Here E_m and k, respectively, represent the peak amplitude of the electric field and the wave number of IASW. The wave number is evaluated by $k = 2\pi/(x_1 - x_2)$, such that $x_2 - x_1$ represents the width of potential structure. As the trapping velocity depends on the maximum strength of electric field linked with IA structures, the electron trapping is affected throughout the breaking and evolution of IASWs. In addition, we estimated the phase velocity (V_s) of the IASW pulse, which is propagating toward the right-side boundary of the simulation. Electrons having velocities within $V_{trap} - V_s$ and $V_{trap} + V_s$ can get trapped within the potential structure. Thus, the maximum trapping velocity of the electron is given by the sum of trapping and phase velocity ($V_{trap} + V_s$). The variation of maximum trapping velocity as a function of time is shown in Fig. 5(b) for both simulation Run-1 (red color) and Run-2 (blue color). Vertical dashed lines in Fig. 5 represent the times of formation and breaking of IASWs in simulation Run-1 (red color) and Run-2 (blue color).

Overall Fig. 5 gives time variation of the maximum electric field and the maximum electron trapping velocity for both simulation runs. The maximum electric field initially increases with time and then attains the first maxima at time $\omega_{pi}t_{F1} = 38$ in Run-1 and $\omega_{pi}t_{F1} = 46$ in Run-2. The amplitude of the electric field further increases again and attains the second maxima at the time of steepening of the IASW pulses. Subsequently, after attaining the maximum steepening, the IASW pulses break, which resulted in decreasing of the wave amplitude. After breaking of the initially generated IASW pulses in both runs, the newly generated pulses detached from each other to form chains of IASW pulses. In these chains, the amplitudes of the leading pulses are larger than those of the backward pulses. After the wave breaking, the increasing trend of the IASW amplitude in Fig. 5(a) is due to the increasing amplitude of the leading IASW pulses in the system. An interesting feature is seen in the maximum electron trapping velocity. It shows two peaks: first at the time of initial formation of IASW pulses, and second at the time of breaking of the IASWs. It is seen that the $V_{trap} + V_s$

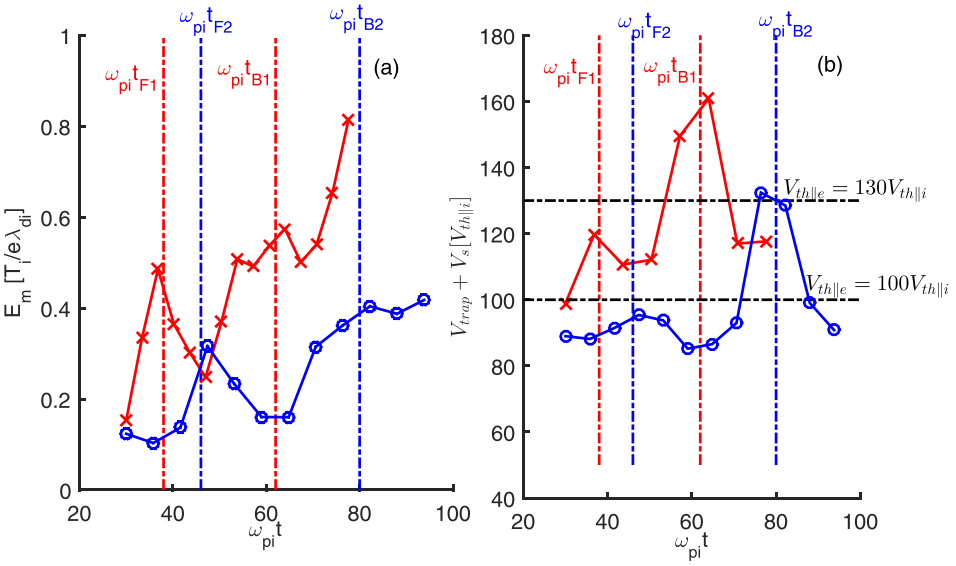

FIG. 5. Time variation of (a) maximum electric field amplitude of the leading IASW pulse, (b) sum of trapping velocity, and phase velocity of the leading pulse; given by $V_{trap} + V_s$ for Run-1 and Run-2. The dashed vertical lines at time step $\omega_{pi}t_{F1}$ and $\omega_{pi}t_{F2}$ show formation of two counter-propagating IASW pulses in Run-1 and Run-2, respectively. The dashed lines at $\omega_{pi}t_{B1}$ and $\omega_{pi}t_{B2}$ show the time steps at which the initiation of the IASW breaking takes place in Run-1 and Run-2, respectively. The horizontal lines show the thermal velocity of electrons for Run-1 (red) and Run-2 (blue).

consistently increases, and crosses the electron thermal velocity during steepening of the IASW pulses. The $V_{trap}+V_s$ attains the critical threshold of the trapping velocity at time $\omega_{pi}t_{B1}=62$ in Run-1 and at $\omega_{pi}t_{B2}=80$ in Run-2, when the initially formed IASWs start to break.

C. Ponderomotive processes at the breaking of IASWs

As mentioned in Sec. III A, the introduction of IDP with an equal electron and ion density creates spatially varying electric field due to charge separation. In the presence of spatially varying electric field, i.e., $E(x,t)=E_m(x)\cos(\Omega t)$, the electrons and ions experiences the ponderomotive force ($F_p=-q\nabla\Psi$). The associated potential of the electron is given by following equation:[16]

$$\Psi_e=\frac{1}{4}\frac{e}{m_e\Omega^2}|E|^2=\frac{1}{2}\frac{e}{\varepsilon_0 m_e\Omega^2}U. \tag{3}$$

In the equations above, e is the electrical charge of the electron, m_e is its mass, Ω is the angular frequency of oscillation of the field, E is the amplitude of the electric field, Ψ is the ponderomotive potential, and U is electrostatic energy. It should be noted that for computing the ponderomotive potential using Eq. (3), we used the estimates of ponderomotive frequency, which is given by Kakad and Kakad[16]

$$\Omega^2=\frac{U}{KE_e}\frac{\omega_{pe}^2}{4}, \tag{4}$$

where KE_e is the electron kinetic energy. In a similar way, we can obtain the ponderomotive frequencies from the ion ponderomotive force. To understand the breaking of the IASWs, we followed the average ponderomotive frequencies and the maximum ponderomotive potential associated with the electrons and the ions in the simulation system. These physical quantities obtained from Run-1 and Run-2 are shown in Fig. 6. Here our aim is to examine the evolution of the maximum ponderomotive potential and frequency during the formation and breaking of IASWs. It may be noted that the ponderomotive potential is charge dependent, and hence we expect negative (positive) ponderomotive potential for electrons (ions). However, while computing the maximum ponderomotive potential for electrons we have considered its absolute values. In a recent study using fluid simulations, it is shown that ponderomotive potential shows a two-peak structure, in which first (second) peak is seen close to the time of formation (breaking) of IASWs.[16] Similar to that, we observe two-peak structures in the maximum ponderomotive potential of both electrons and ions in the present simulation. The vertical dashed-dotted lines at times $\omega_{pi}t_{F1}$ and $\omega_{pi}t_{F2}$ shown in the panels of Fig. 6 represent times at which the two IASW pulses formed initially, whereas the vertical dotted lines at $\omega_{pi}t_{B1}$ and $\omega_{pi}t_{B2}$ represent the times at which the breaking of the IASW initiate in Run-1 and Run-2, respectively.

Both electron and ion maximum ponderomotive potentials depicted in Figs. 6(c) and 6(d) show the similar trend at the different stages involved during the evolutions and breaking of the IASWs in both Run-1 and Run-2. It is seen that both $|\Psi_{m,ele}|$ and $|\Psi_{m,ion}|$ remain nearly invariable for few initial time steps (i.e., $\omega_{pi}t<0.7$), which later oscillates till $\omega_{pi}t\leq 30$, and then decreases until $\omega_{pi}t\approx 70$. Later, both electron and ion maximum ponderomotive potentials quickly increased with time and attain peak at the formation of two initial IASW pulses, i.e., $\omega_{pi}t_{F1}$ in Run-1 and $\omega_{pi}t_{F2}$ in Run-2. After this maximum, both ponderomotive potentials in the system start decreasing and reached the minimum. Later, both electron and ion ponderomotive potentials in the system increase during the steepening of the IASW pulse, and they attain the maximum at the time of breaking of the IASW pulses i.e., $\omega_{pi}t_{B1}$ in Run-1 and $\omega_{pi}t_{B2}$ in Run-2. This shows similar characteristics of the electron and ion ponderomotive potentials at the times of formation and breaking of IASW pulses, which are observed in the fluid simulation of the breaking of IASWs.[16] Furthermore, we investigate the time evolution of the average ponderomotive frequencies obtained from electrons and ion kinetic energies, which is depicted in Figs. 6(a) and 6(b), respectively. These figures show that the average ponderomotive frequencies of both ions and electrons have larger values initially. It is observed that the electron and ion ponderomotive frequencies gradually (rapidly) increase till the initiation of the steepening (during the steepening and breaking) of IASW pulses. The increasing trend of the ion and electron ponderomotive frequencies at the steepening and breaking of the IASWs is analogous to the characteristics of the ponderomotive frequencies reported by Kakad and Kakad.[16]

D. Particle acceleration/deceleration at the breaking of IASWs

In this section, we examine changes in distribution functions of electrons and ions during the formation and evolution of the IASWs. This is carried out to understand the connection between the particle acceleration/deceleration during and after the breaking of the IASWs. For this purpose, the initial distribution function at $\omega_{pi}t=0$ is subtracted from the distribution function at a given time $\omega_{pi}t$ for each species to obtain the variation in the distribution function, i.e., $[\Delta f(V)]_j$. The time evolution of the changes in the ion and electron distribution functions for Run-1 (Run-2) are presented, respectively, in Figs. 7(a) and 7(b) [Figs. 7(c) and 7(d)]. In both runs, it is seen that the ions with lower velocities are accelerated to the higher velocities during the initial formation of two IASW pulses. At the same time, some of the electrons with the higher velocities are decelerated to the lower velocities. As discussed in Sec. III B, the wave breaking initiates around $\omega_{pi}t=62$ and $\omega_{pi}t=80$ for Run-1 and Run-2, respectively. At a later time, these newly formed IA pulses in the chain of IASWs separate from each other since they travel with different phase velocities. These IA pulses are distinct and keep evolving to achieve stability, i.e., soliton type characteristics. During the process, they shed some mass of trapped electrons, which is clearly evident in the movies (given as the supplementary material). As these vortices of trapped electrons having different phase velocities move in an unperturbed plasma, the electrons are accelerated

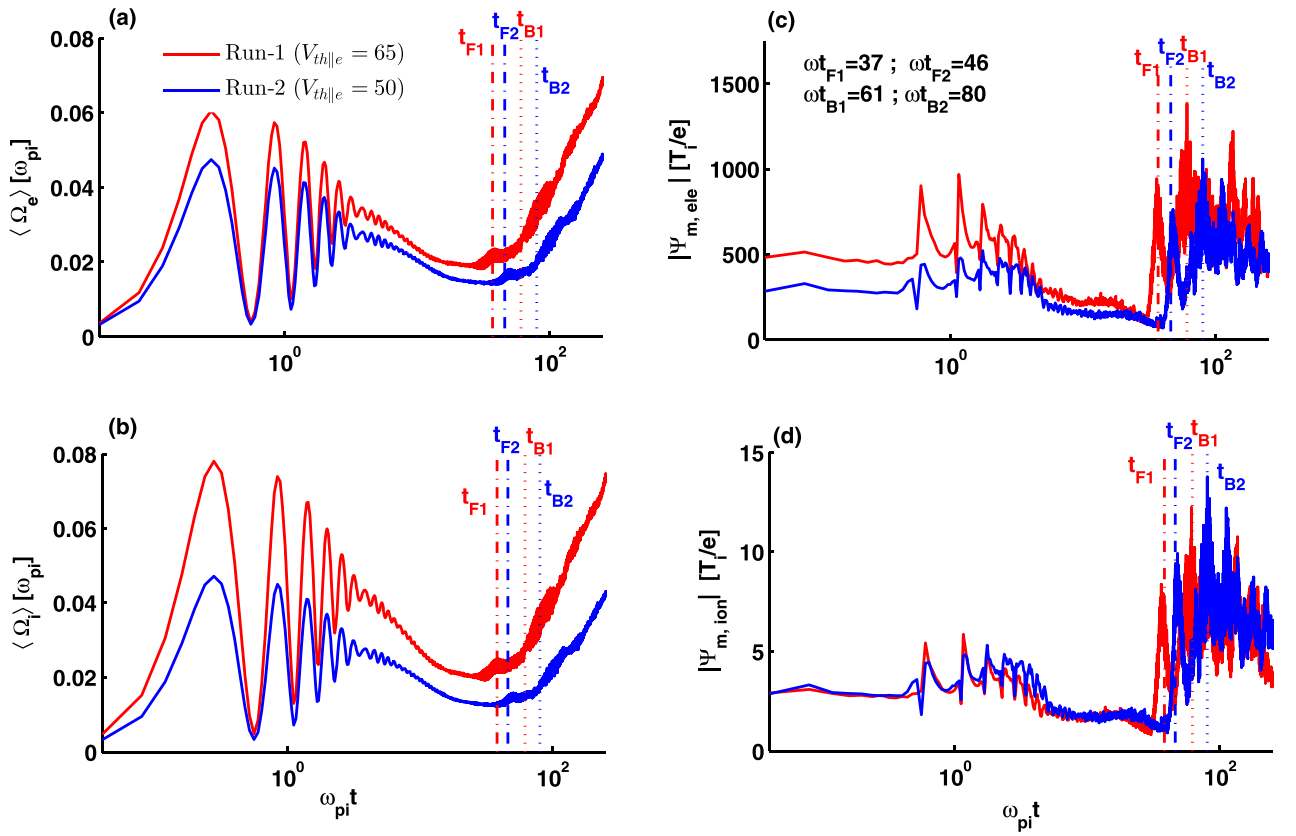

FIG. 6. Time variation of (a) average electron ponderomotive frequency, (b) average ion ponderomotive frequency, (c) maximum electron ponderomotive potential, and (d) maximum ion ponderomotive potential for Run-1 and Run-2. The vertical dashed lines at time $\omega_{pi}t_{F1}$ and $\omega_{pi}t_{F2}$ show formation of two counter-propagating IASW pulses in Run-1 and Run-2, respectively. The lines at $\omega_{pi}t_{B1}$ and $\omega_{pi}t_{B2}$ show the time steps at which the initiation of the breaking of IASWs takes place in Run-1 and Run-2, respectively.

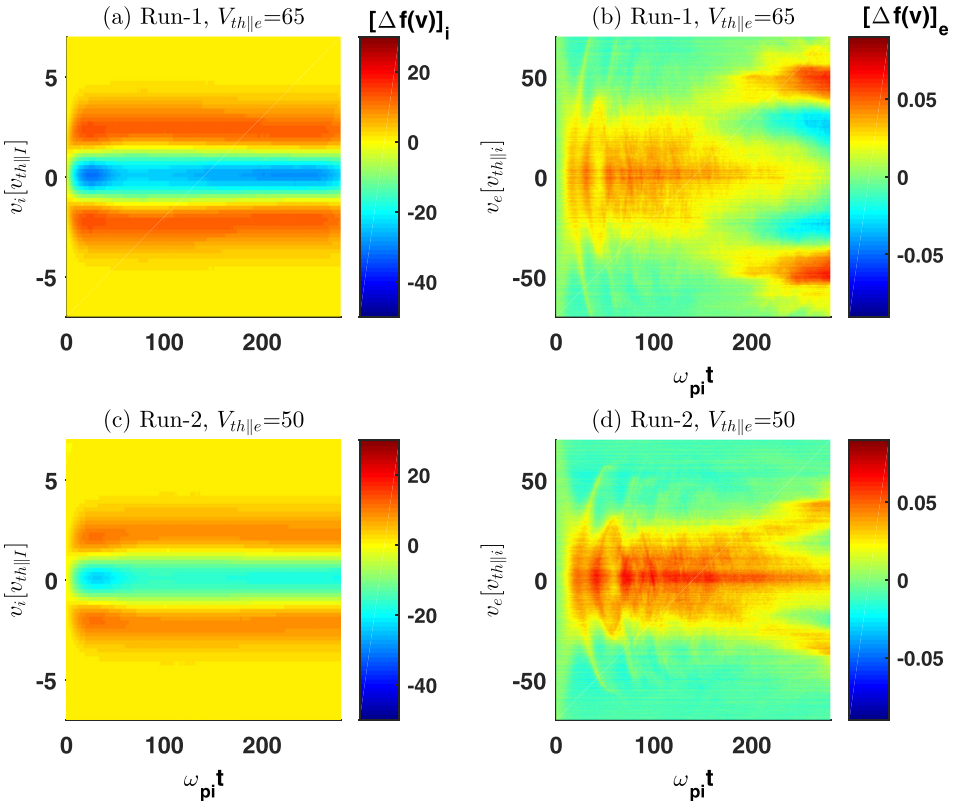

FIG. 7. Time evolution of change in distribution function as compared to its initial distribution (i.e., $[\Delta f(V)]_j$) for (a) ions, Run-1, (b) electrons, Run-1, (c) ions, Run-2 and (d) electrons, Run-2.

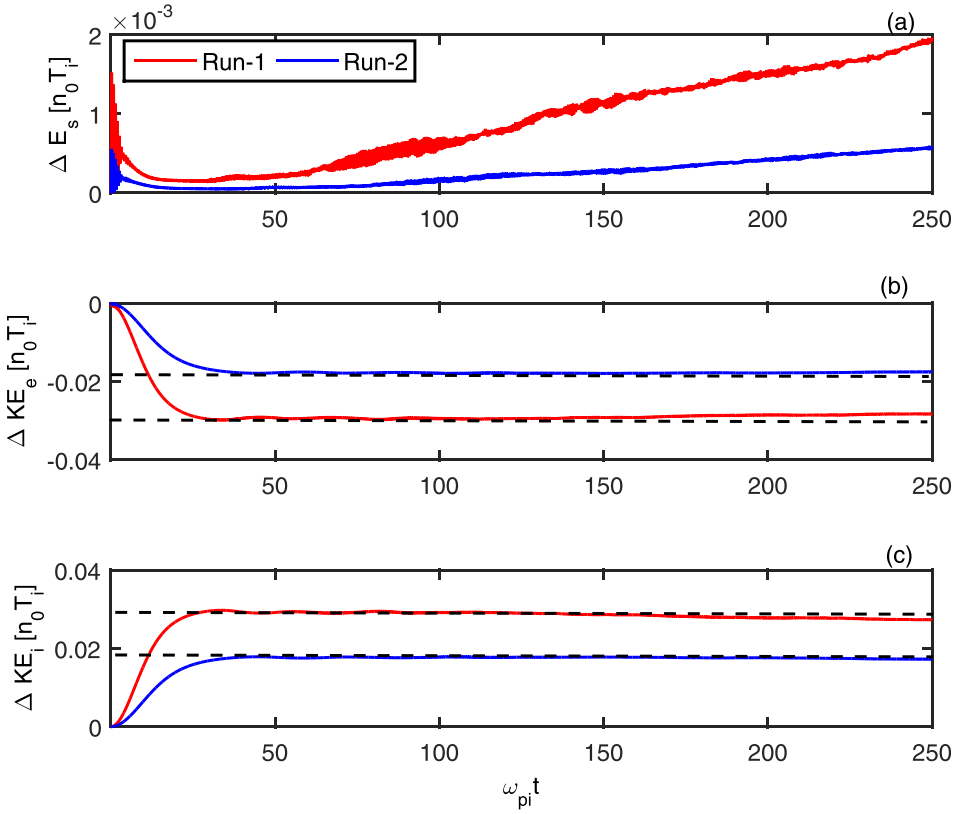

FIG. 8. Evolution of change in (a) electrostatic energy, (b) electron kinetic energy, and (c) ion kinetic energy as a function of time for Run-1 and Run-2.

at $\omega_{pi}t = 170$ and $\omega_{pi}t = 220$ for Run-1 and Run-2, respectively.

We have also examined the changes in electrostatic energy and kinetic energies of the electrons and ions with time for both simulations runs discussed here. For this purpose, the energies at $\omega_{pi}t = 0$ are subtracted from the corresponding estimates of electrostatic and kinetic energies at other time to obtain the change in these energies. Figures 8(a), 8(b), and 8(c), respectively, show the time variations of changes in electrostatic energy (ΔE_s), electron kinetic energy (ΔKE_e), and ion kinetic energy (ΔKE_i). It is seen that the electrostatic energies in both simulation runs initially increase rapidly, and then decrease at the formation of two IASW pulses in the system. The electrostatic energy was found to increase with the steepening and breaking of the IASWs in the system. The variation in the maximum kinetic energy of the electrons, given in Fig. 8(b), shows that the electrons lose kinetic energy in the course of formation of two IASW pulses. At the same time, it is seen that the maximum kinetic energy of the ions increases during initial formation of IASW pulses, which is displayed in Fig. 8(b). It is noted that the energy exchange between ion and electron energies during the formation of IASWs occurs earlier in plasmas having higher thermal velocities.

IV. SUMMARY AND CONCLUSIONS

We perform one-dimensional PIC simulations to investigate the breaking of the IASWs in plasmas. We initialize the simulation by superimposing the long-wavelength perturbation into electron and ion equilibrium densities as defined by Kakad *et al.*[15] We find that the IDP in the plasma initially evolves into the long-wavelength IASW pulses along with the IA oscillations and Langmuir waves. Later, the simulation shows that the long-wavelength IASWs steepen, break, and evolve into the chain of coherent IASW pulses in the system. We have discussed the generation of nonlinear IASW pulses through the breaking of the long-wavelength IASWs, with a particular emphasis placed on the criteria of wave breaking. We have examined the electron trapping and ponderomotive processes during the generation and evolution of IASWs and established the criteria for breaking of the IASWs. It is known that the particle trapping velocity is proportional to a square root of IASW amplitude. The amplitude of IASWs formed in the higher (lower) electron temperature plasma is larger (smaller). Therefore, the trapping velocity is found to be greater in the simulation run with the larger electron temperature as compared to those with the smaller electron temperature. A larger trapping velocity indicates the trapping of a larger number of electrons in the IASW potential. Our simulations illustrate that the maximum trapping velocity ($V_{trap} + V_s$) attains the first peaks at the time of formation of two IASW pulses, and the second peak at the time of their breaking. The trapping velocity at the time of the formation of two pulses (i.e., first peak) is less than the electron thermal velocity, whereas it exceeds the electron thermal velocity at the second peak where IASW pulse breaks. In practice, plasma waves can support a certain number of trapped electrons without losing the wave structure. These trapped particles may cause the wave to be Landau damped. As long as the wave structure remains intact however, the wave cannot be considered broken. It is seen that V_s is much smaller compared to the trapping velocity and thermal velocity of the electron. Thus, one can conclude that an IASW

pulse breaks when $V_{trap} > V_{the}$ in both simulation runs. In other words, it indicates that an IASW pulse breaks when the maximum work done by trapped electrons under the influence of electrostatic potential linked with IASW exceeds the electron thermal energy, i.e., $qE_0\lambda > 0.5m_eV_{the}^2$.

The electron and ion ponderomotive potentials are established as proxies to identify the initiation of IA wave breaking in fluid treatment of plasmas.[16] Our simulations demonstrate the overall behaviour of the ponderomotive potentials and ponderomotive frequencies of the electrons and ions in the course of evolution of IASWs in plasma. Both electron and ion ponderomotive potentials attain the first maxima near the formation of the initially generated two long-wavelength IASW structures, and the second maxima at the time of the initiation of the breaking of these long-wavelength IASW structures. In addition, it is noticed that the ponderomotive frequencies of the electrons and ions remain unchanged from the time of formation of the long-wavelength IASW up to the time of the initiation of their steepening. Later, during steepening of these IASWs, the electron and ion ponderomotive frequencies increase again. Based on the present work, we proposed that the time variation of electron and ion ponderomotive potentials and the ponderomotive frequencies can be used as proxies for determining the steepening and breaking times of the IASWs in the kinetic model.

It is known that the IDP parameters and the electron temperature in the simulation have an influence on the characteristics of the generated IASW pulses. Both amplitude and phase velocity of the IASW structures formed through the wave breaking process, and those appear as a chain of coherent phase-space vortices are higher for plasmas having higher electron thermal velocities. Furthermore, the number of IASW structures formed through the wave breaking process is dependent on the electron thermal velocities. The chain of IASWs contains less (more) number IASW pulses in the plasmas with higher (lower) electron thermal velocities.

SUPPLEMENTARY MATERIAL

See supplementary material for the animation of formation of multiple counter-propagating coherent phase space structures associated with the IASWs in a plasma for Run-1 and Run-2.

ACKNOWLEDGMENTS

This study was supported by an Indo-Japanese bilateral research project. The model computations were performed on the High Performance Computing System at the Indian Institute of Geomagnetism.

[1]C. Maity, A. Sarkar, P. K. Shukla, and N. Chakrabarti, Phys. Rev. Lett. **110**, 215002 (2013).
[2]A. I. Akhiezer and R. Polovin, Sov. Phys. JETP **3**, 696 (1956).
[3]J. M. Dawson, Phys. Rev. **113**, 383 (1959).
[4]T. Coffey, Phys. Fluids **14**, 1402 (1971).
[5]W. L. Kruer, Phys. Fluids **22**, 1111 (1979).
[6]A. Bergmann and P. Mulser, Phys. Rev. E **47**, 3585 (1993).
[7]S. Pramanik, C. Maity, and N. Chakrabarti, Phys. Plasmas **21**, 022308 (2014).
[8]T. Katsouleas and W. Mori, Phys. Rev. Lett. **61**, 90 (1988).
[9]J. Rosenzweig, Phys. Rev. A **38**, 3634 (1988).
[10]C. Schroeder, E. Esarey, and B. Shadwick, Phys. Rev. E **72**, 055401 (2005).
[11]S. Alikhanov, R. Sagdeev, and P. Chebotaev, Sov. Phys. JETP **30**, 847 (1970).
[12]C. Judice, J. Decker, and R. Stern, Phys. Rev. Lett. **30**, 267 (1973).
[13]D. Forslund, J. Kindel, K. Lee, and B. Godfrey, Phys. Fluids **22**, 462 (1979).
[14]P. Rosenau, Phys. Fluids **31**, 1317 (1988).
[15]A. Kakad, Y. Omura, and B. Kakad, Phys. Plasmas **20**, 062103 (2013).
[16]A. Kakad and B. Kakad, Phys. Plasmas **23**, 122101 (2016).
[17]S. Hosseini Jenab and F. Spanier, Phys. Plasmas **23**, 102306 (2016).
[18]A. Kakad, B. Kakad, and Y. Omura, Phys. Plasmas **24**, 060704 (2017).
[19]Y. Omura and H. Matsumoto, *Computer Space Plasma Physics: Simulation Techniques and Software* (Terra Scientific Publishing Company (TERRAPUB), Tokyo, 1993), Chap. 2, p. 21.
[20]B. Kakad, A. Kakad, and Y. Omura, J. Geophys. Res.: Space Phys. **119**, 5589, doi:10.1002/2014JA019798 (2014).
[21]Y. Omura, H. Kojima, and H. Matsumoto, Geophys. Res. Lett. **21**, 2923, doi:10.1029/94GL01605 (1994).
[22]Y. Omura, *Advanced Methods for Space Simulations*, edited by H. Usui and Y. Omura (Terra Sci., Tokyo, 2007), 1 (2007).
[23]H. Matsumoto and Y. Omura, J. Geophys. Res.: Space Phys. **86**, 779, doi:10.1029/JA086iA02p00779 (1981).